International Journal of Heat and Mass Transfer 221 (2024) 125012

Contents lists available at ScienceDirect

International Journal of Heat and Mass Transfer

journal homepage: www.elsevier.com/locate/ijhmt

Topological data analysis of TEM-based structural features affecting the thermal conductivity of amorphous Ge

Yen-Ju Wu [a], Kazuto Akagi [b,*], Masahiro Goto [c], Yibin Xu [a,*]

[a] Center for Basic Research on Materials, National Institute for Materials Science (NIMS), 1-2-1 Sengen, Tsukuba, Ibaraki 305-0047, Japan
[b] Advanced Institute for Materials Research, Tohoku University, 2-1-1 Katahira, Aoba, Sendai 980-8577, Japan
[c] Research Center for Materials Nanoarchitectonics (MANA), National Institute for Materials Science (NIMS), 1-2-1 Sengen, Tsukuba, Ibaraki 305-0047, Japan

ARTICLE INFO

Keywords:
Amorphous materials
Topological data analysis
Atomic network
Structure feature
Thermal conductivity

ABSTRACT

Compared to crystalline materials, amorphous materials lack periodicity and exhibit distinct thermal and lattice vibration properties. Hence, analyzing atomic networks in the transmission electron microscopy (TEM) images of amorphous materials is challenging. In this study, we employ topological data analysis (TDA) and principal component analysis (PCA) to extract structural features from the TEM images of amorphous germanium (a-Ge) and analyze its atomic networks. Our findings demonstrate that the thermal conductivity of a-Ge is influenced by larger atomic rings with more vertices, which facilitates the heat transfer through longer atomic chains and results in a higher thermal conductivity. A comparison of the experimental and simulation data confirms the non-random nature of the atomic arrangements in a-Ge. We propose herein an approach that employs the TDA to identify and analyze the atomic networks in amorphous materials, establishing connections to their thermal properties. This study enhances our understanding of amorphous materials and paves a way for tailored material design and engineering to achieve the desired thermal properties.

1. Introduction

Due to their thermal properties, amorphous materials are attracting increasing attention for use in flexible electronics [1,2], artificial intelligence chips [3], thermal protection [4], advanced detectors [5], and thermoelectrics [6,7]. The lattice vibration and the temperature dependence of the thermal properties of amorphous materials that lack periodicity are significantly different from corresponding crystalline materials. Propagons, diffusons, and locons originally introduced by Einstein [8] and refined by Slack [9], Cahill et al [10,11]., and Allen and Feldman [12,13] are often used to describe thermal transport mechanisms and predict the thermal conductivity of various amorphous materials [14]. Allen et al. proposed propagons, diffusons, and locons as three types of vibrational modes in amorphous materials that thoroughly explain the temperature dependence of the thermal conductivity of amorphous Si [15]. Propagons are plane wave-like delocalized vibrational modes at low frequency; diffusons are delocalized vibrational modes in a large frequency range; and locons are localized vibrational modes. Diffusons comprise the majority of and dominate heat transport in amorphous materials. Theoretical approaches to understanding thermal transport in amorphous materials have been discussed in the recent literatures [16,17].

The contributions of different vibrational modes to thermal conductivity are strongly correlated to the atomic network that changes the vibrational states of amorphous materials [18,19]. Several approaches are used to manipulate the atomic network of amorphous materials. These include the introduction of impurities, composition change (i.e., varying the stoichiometry), and mass density tuning. Prior results demonstrated that decreasing the coordination or bonding number by introducing impurities in the Si [20], SiO [20], and SiC [21] amorphous films reduces their thermal conductivities. Another approach is to increase the Te content in amorphous SiTe, which reduces the coordination number, results in a large mobility edge shift, and suppresses the contributions of propagons and diffusons to thermal conductivity [22]. Mass density tuning from 2.0 to 3.4 g/cm^3 is also another approach of manipulating the coordination number and the sp^2/sp^3 bond ratios in amorphous carbon, which changes the thermal conductivity from 0.65 to 1.05 W/mK [23].

The medium-range order (MRO) referred to as the 0.5–5 nm atomic arrangement is found in various amorphous materials [5,24-26] and significantly affects a material's physical properties. Understanding the correlation between an atomic network and thermal conductivity is

* Corresponding authors.
E-mail addresses: kazuto.akagi.b5@tohoku.ac.jp (K. Akagi), Xu.Yibin@nims.go.jp (Y. Xu).

https://doi.org/10.1016/j.ijheatmasstransfer.2023.125012
Received 25 September 2023; Received in revised form 10 November 2023; Accepted 24 November 2023
Available online 6 December 2023

critical for thermal management. However, the nonperiodic atomic network in amorphous materials makes it complicated to define the structural features and construct the simulation models. Conventional X-ray diffraction has shown that amorphous materials have no sharp diffraction Bragg peaks or rings. The radial distribution function, also known as the pair distribution function (PDF), obtained from electron diffraction is used to interpret the local structure (e.g., MRO in amorphous materials) [5,27-29]. However, interpretation is not simple because of the convoluted PDF information of various bonds/pairs with similar distances [29]. The influence of inelastically scattered electrons on the diffraction intensity must be removed to obtain detailed structural information (e.g., coordination number) [30].

Topological data analysis (TDA) uses persistent homology to quantify the shape of data with the information of "holes". If a set of discrete points is given and we put circles (or spheres) with the common radius at each point, the 1st-order holes (rings) characterizing this system are recorded as a set of birth-death events of rings with increase of the radius. Here, the radius when two circles contact at the longest edge and form a polygon is called "birth time", and the radius when the center of the polygon is filled is called "death time". The birth–death pairs shown as a two-dimensional scatter plot is called persistence diagram (PD) [31]. Since PD is useful to describe multiscale topological features (e.g., rings and cavities) of complex atomic configurations, TDA has become popular to analyze the structural features of amorphous materials [32]. Prior reports demonstrated that the TDA can extract structural features to capture the hidden MRO of amorphous materials (e.g., Cu–Zr metallic glass [33], silica glass [32], and ice [34]). Sørensen et al. deconvoluted the contribution of various MRO features to the first sharp diffraction peak in oxide glasses via the TDA [35]. Minamitani et al. determined the relationship among local coordination, atomic network, and thermal conductivity using the topological features of amorphous carbon [23] and amorphous Si [36].

In contrast to the atomic network analysis of the thermal conductivity of amorphous materials using molecular dynamics (MD) simulated models and the TDA, we found the thermal conductivity change in amorphous Ge (a-Ge) by varying the experimentally deposited temperatures [37,38]. In our previous work, the presence of the short-range order in a-Ge was revealed by the fast Fourier transform patterns of the TEM images [38]. The a-Ge films deposited at higher temperatures were more locally ordered than those deposited at room temperature. Without introducing impurities or changing the chemical compositions, which are closely related to the thermal properties, we could identify the effect of the atomic network on the thermal conductivity change. The higher thermal conductivity was attributed to the short-range structural order at a 2–3 nm scale in a-Ge thin films, which facilitated the heat transfer from one atom to the atoms beyond its nearest neighbor.

Our previous results provided experimental evidence for understanding the underlying nature of the mean free path variation in amorphous solids [37,38]. However, the appropriate structural features, atomic network corresponding to the short-range order, and associated physical properties of thermal conductivity are still lacking. In this study, we apply the TDA to identify the structural feature from the observed TEM (TEM-structural feature). Note that the TEM images provide the atomic structural information of crystalline materials while that is interference with higher amount of diffuse scattering due to the nonperiodicity in amorphous materials. Thus, the structural features extracted from the TEM images of amorphous materials become convolutional information. In other words, they project a disordered atomic structure of a three-dimensional (3D) unit cell on a two-dimensional (2D) space.

The TEM-structural feature allows us to describe the differences of the atomic network in a-Ge thin films deposited at various temperatures. The a-Ge model generated using Ab Initio Molecular Dynamics (AIMD) simulations was used to perform a comparison with the experimental samples. In this study, we have successfully identified TEM-based structural features that distinguish amorphous materials, allowing us to describe their atomic networks. This structural characterization technique is not limited to the specific material analyzed here but has broader applicability to various amorphous materials. The principles and methodologies we have applied are transferable to other materials and can be employed in real experiments using TEM, making it a valuable tool for the analysis of a wide range of amorphous systems. Our results provide an avenue for defining the atomic network characteristics of amorphous materials through TEM-structural features.

2. Results and discussion

The TDA was performed to extract the structural features of the samples listed in Table 1. The simulation-based samples were compared with the experimental ones. The sample selection was designed to encompass a diverse range of conditions and variations, enabling a comprehensive analysis and facilitating comparisons between the experimentally obtained samples and simulated scenarios.

A. Preprocessing and data cleaning of TEM images

The Ge25 TEM images underwent various steps to enhance quality and extract relevant information. Fig. 1 provides an overview of this process. Artwork (a) depicts a TEM image of the Ge deposition on a Si substrate, where the ~2.3 nm native oxide layer on the Si substrate was intentionally retained. This image serves as the initial sample representation. In (b), an atomic-resolution TEM image of the a-Ge is presented. The scale and the aspect ratio of the a-Ge image were adjusted with respect to c-Si, a reference material, to ensure an accurate analysis. This correction step helped maintain the proper dimensional proportions for the subsequent analysis. More importantly, the point cloud data obtained from the TEM images of the crystalline materials denoted atomic structural information. In the case of the amorphous materials, the data became convoluted due to nonperiodicity. As inferred from the number of birth–death pairs, the Ge25 density was approximately 7% higher than the Ge100 and Ge300 densities. Accordingly, the extracted structural features from the TEM images of the amorphous materials represented a disordered atomic structure projection onto a 2D space.

The structural features were quantitatively extracted through the TDA and a set of point cloud data illustrating the relatively bright areas as the death points for the 0th-order homology depicted in Fig. 1(c) (red symbols). Before the TDA, a Gaussian distribution with a 5 px standard deviation was employed for noise reduction. The extraction process resulted in the formation of a massive point cloud (Fig. 1(d)). Subsequently, a series of preprocessing and data cleaning steps were applied to the Ge25, Ge100, and Ge300 TEM images. The enhanced relevant features for further analysis were then prepared as three point cloud data sets. In our analysis, we identified 29,412 bright points from the TEM image of Ge25, covering an area of 2667 nm^2. The term 'Rand' in

Table 1
List of the a-Ge samples for the TDA.

Sample	Method	Description
Ge25	Experiment (TEM)	Deposition temperature: 25 °C
Ge100	Experiment (TEM)	Deposition temperature: 100 °C
Ge300	Experiment (TEM)	Deposition temperature: 300 °C
MDGe3.5	Simulation (AIMD)	2D projected atomic positions in a slice with 3.5 Å thickness
MDGe4.0	Simulation (AIMD)	2D projected atomic positions in a slice with 4.0 Å thickness
MDGe4.5	Simulation (AIMD)	2D projected atomic positions in a slice with 4.5 Å thickness
Rand	Random	Randomly generated point cloud
Rand_hd	Random	Randomly generated point cloud with a higher density (1.5 times of Rand)

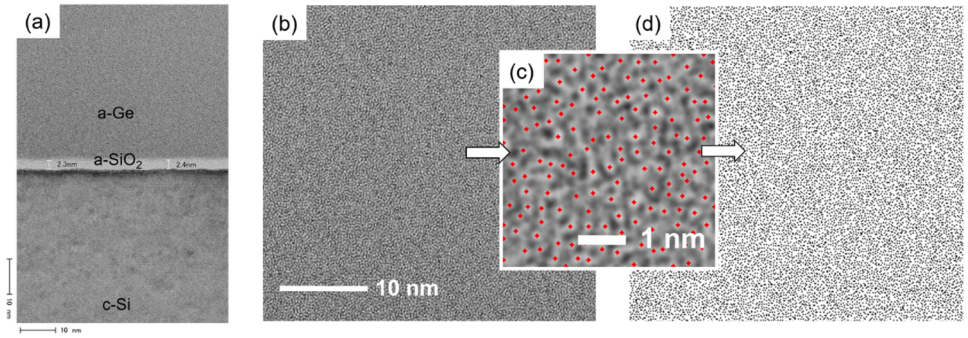

Fig. 1. Transmission electron microscopy (TEM) images and point cloud data representing a structural feature of Ge25: (a) TEM image of the Ge deposition on a Si substrate with the retained ~2.3 nm native oxide layer; (b) atomic-resolution TEM image of a-Ge with the scale and the aspect ratio adjusted relative to c-Si; and (c) death point extraction for the 0th-order homology (red symbols) from (b), which led to the formation of the point cloud dataset (d). (For interpretation of the references to colour in this figure legend, the reader is referred to the web version of this article.)

Table 1 corresponds to the number of points generated randomly within the same area. On the other hand, 'Rand_hd' represents a point cloud with a density 1.5 times higher (= 44,118 points).

B. Application of TDA to identify the local atomic arrangements

We applied the TDA to investigate and identify the local atomic arrangements within the a-Ge samples. Figs. 2–5 provide insights into the structural features and the variations observed at different deposition temperatures. Fig. 2 showcases the point cloud data and the first-order PDs of Ge25, Ge100, and Ge300. The PDs obtained from the point cloud data of the TEM images were calculated and divided into several regions to visually classify the birth–death pairs into polygons from a triangle (three-membered ring) to a hexagon (six-membered ring). A notable trend became evident as the deposition temperature increased: the number of rings with five or six vertices also increased (Figs. 2(d)–(f)), suggesting that higher deposition temperatures contribute to the formation of larger ring atomic structures within the a-Ge samples.

Fig. 3 further illustrates the birth and death value distribution in the first-order PDs for Ge25, Ge100, and Ge300. Figs. 3a-c are obtained by projecting the PDs (Figs. 2d-f) to the birth (or death) axis. Interestingly, in Fig. 3(a), the PDs exhibited a sharper distribution indicating a dominant single order at the lower deposition temperatures for Ge25. In contrast, a broader distribution was observed at the higher deposition temperatures for Ge300 in Fig. 3(c), demonstrating the growth of a new order characterized by a shoulder at higher birth and death values in the local atomic arrangements. The presence of this additional order may have contributed to the enhanced thermal conductivity observed in the samples deposited at higher temperatures. In other words, the deposition temperature plays a crucial role of influencing the complexity and the diversity of the atomic structures within the a-Ge samples.

We investigated the deposition temperature dependence of the atomic networks by conducting a PCA of the PDs. PCA is one of the dimensionality reduction methods based on linear algebra. It gives the axes (principal component vectors) in N-dimensional space which emphasize difference among the input vectors and enables us to extract

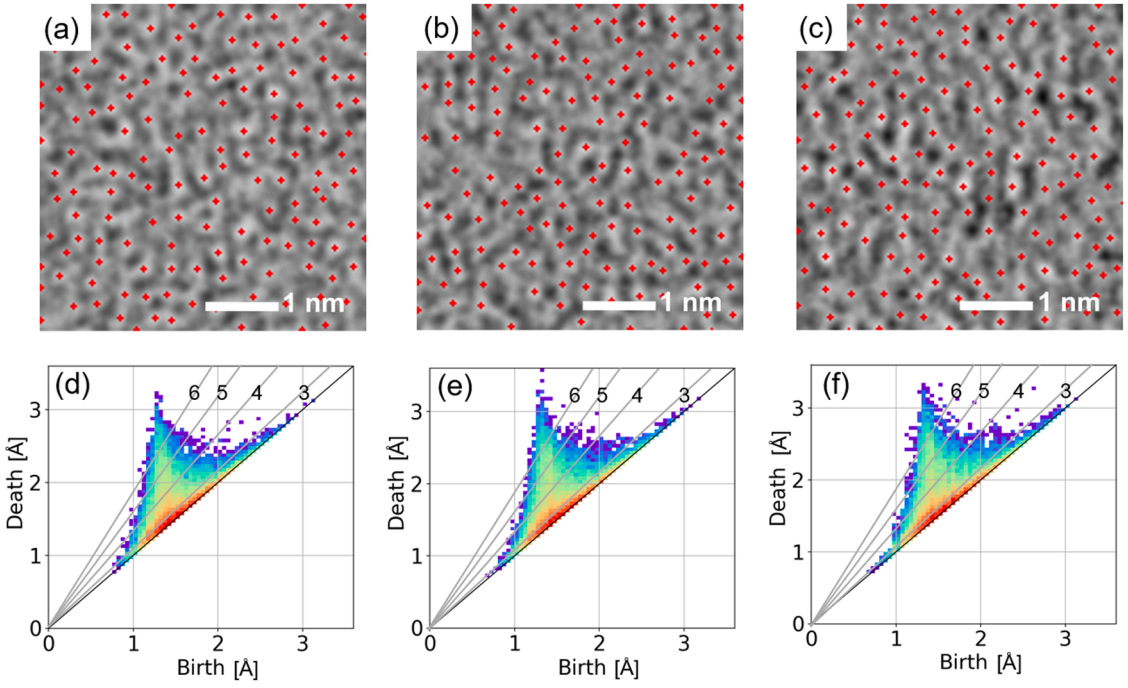

Fig. 2. Images of the point cloud data (upper) and the first-order PDs (bottom) of the amorphous Ge samples: (a, d) Ge25, (b, e) Ge100, and (c, f) Ge300. The number of rings with five or six vertices increased as the deposition temperature increased. (d, e, f) The birth–death pairs over the lines labeled as n (n = 3 to 6) were larger than those in the n-membered ring. The PD color indicates the density of the birth–death pairs, which ranged from red to purple, as the density decreased. (For interpretation of the references to colour in this figure legend, the reader is referred to the web version of this article.)

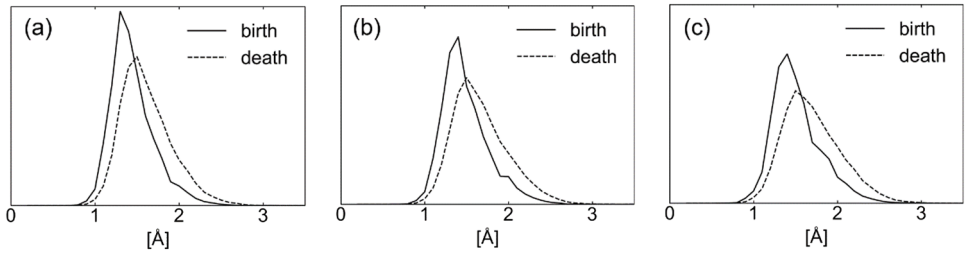

Fig. 3. Distribution of the birth and death values in the first-order PDs for (a) Ge25, (b) Ge100, and (c) Ge300. The y-axis shows the number of rings at the given birth (or death) value. In Figs. 3a-c, the same scale of y-axis is used to clarify the difference among the samples. The PDs exhibit a sharper distribution indicating a single order at lower deposition temperatures. By contrast, a broader distribution is observed at higher deposition temperatures. These results suggest the possibility of an additional shoulder corresponding to another order with larger rings developing at higher deposition temperatures.

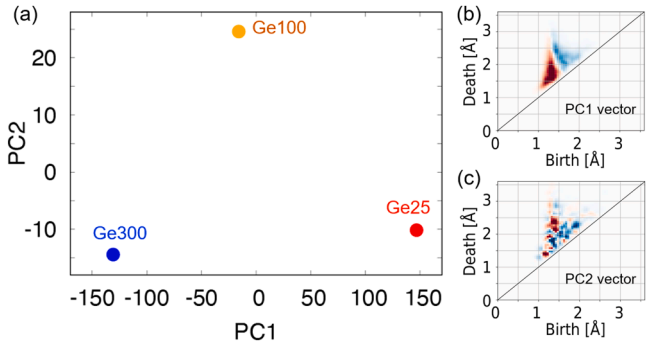

Fig. 4. PCA analysis of the PDs from the a-Ge TEM images: (a) first (PC1) and second (PC2) principal components for a-Ge, Ge25, Ge100, and Ge300. The x and y axes are PCA component scores, represented without specific units, as PCA generates unit-less linear combinations of the original variables. (b, c) PD-like expression of the PC1 and PC2 vectors. For each element in the PC vector, the red color indicates positive signs, while the blue color represents negative signs. The darker color levels correspond to a higher density of the birth–death pairs. The contribution rates of the PC1 and PC2 vectors are 0.977 and 0.023, respectively. The results indicate that larger ring structures are more prevalent at higher deposition temperatures. (For interpretation of the references to colour in this figure legend, the reader is referred to the web version of this article.)

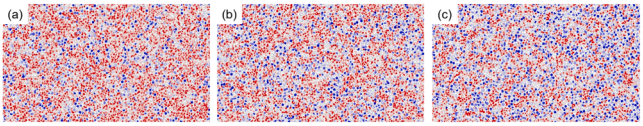

Fig. 5. Inverse analysis of (a) Ge25, (b) Ge100, and (c) Ge300 obtained from the PC1 vector. The ring structure positions represented by the center of death triangle are colored as follows: the red parts indicate the positive components in the PC1 vector, while the blue ones represent the negative components. The emergence of blue networks with the increasing deposition temperature suggests the development of larger ring structures during deposition at higher temperatures. (For interpretation of the references to colour in this figure legend, the reader is referred to the web version of this article.)

critical information from datasets with numerous variables. By projecting a vector onto first and second principal component vectors, its first and second principal component values (PC1 and PC2) are obtained. In this study, each PD was divided into a 2D mesh and converted into a vector, whose element represents the numbers of birth–death pairs in the corresponding mesh. The vector set was used as the input data for the PCA. Fig. 4(a) shows a 2D map quantifying the PDs of Ge25, Ge100, and Ge300 using the first (PC1) and second (PC2) principal component values. The contribution rate of PC1 was 97.7%, while that of PC2 was 2.3%. The dominant contribution rate of PC1 indicated its significance in capturing major structural variations. Figs. 4(b) and (c) illustrate the PD-like expressions of the PC1 and PC2 vectors, offering visual representations of the significant areas in the PDs captured by these principal components. In Fig. S1, the PCA of the 12 vectors generated by the four divisions of each TEM image yielded the same result as in Fig. 4. Thus, it is reasonable to say that PC1 exhibits a strong correlation with the deposition temperature, whereas PC2 does not demonstrate a clear correlation. In Fig. 4(b), the red and blue colors in the reconstructed PDs from the PC1 vector indicate the positive and negative signs, respectively, of each element in the PC1 vector. Correspondingly, the Ge25 (300) sample with a low (high) deposition temperature showed a stronger structural feature, as represented by color red (blue) in the figure.

We investigated the signal origin in the persistence diagrams by performing an inverse analysis to extract the local structural features. Fig. 5 illustrates the ring structure mapping in the point cloud data on Ge25, Ge100, and Ge300. The position of each ring structure is represented by the center of its death triangle. The color scheme in Fig. 4(b) corresponds to the positive and negative values of the PC1 vector elements reflected by the red and blue areas, respectively. The emergence of the blue networks with the increasing deposition temperature suggests the development of larger ring structures during the deposition process at higher temperatures (Fig. 5(c)). This comprehensive analysis of the point cloud data, persistence diagrams, PCA, and inverse analysis provides valuable insights into the structural features and variations present in the a-Ge samples.

C. Comparison with the AIMD simulation model

We employed AIMD simulation models to further explore the local atomic arrangements in a-Ge and complement the experimental findings. Fig. 6 showcases the a-Ge model generated through the AIMD simulation with 1000 atoms. The 3D atomic configuration of a-Ge was

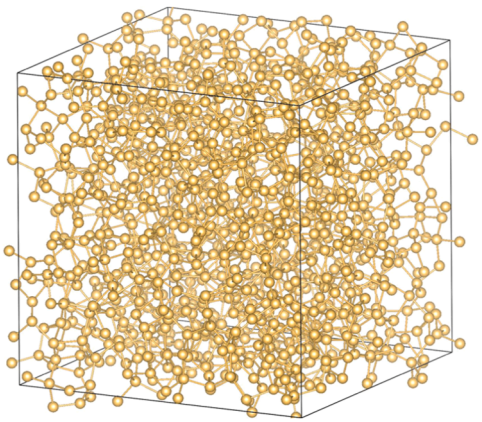

Fig. 6. a-Ge model generated using the molecular dynamics simulation with 1000 atoms.

sliced into 3.5-, 4.0-, and 4.5 Å-thick slabs. A set of point cloud data was then obtained by 2D mapping. We performed the TDA of these point cloud data to compare them with the structural information in the TEM image.

Fig. 7 presents the first-order PDs of the experimental Ge25 sample along with the MDGe4.0, MDGe3.5, and MDGe4.5 AIMD simulation models having 4.0, 3.5, and 4.5 Å thicknesses, respectively. Randomly generated point cloud data referred to herein as Rand and Rand_hd were used for comparison. Fig. S2 illustrates these point cloud data. A notable observation was the similarity in the birth–death pair distribution between Ge25 and the AIMD simulation models shown in Figs. 7(b), (d), and (e). Conversely, the PDs of the random structures in Figs. 7(c) and (f) exhibited much broader birth–death pair distributions. These findings suggest that the experimental Ge25 sample and the AIMD simulation models shared similar local atomic arrangements.

Fig. 8 illustrates the analysis results of the birth–death value distribution in the first PDs. The TEM image displayed narrower birth–death value ranges compared to the random structures, indicating the non-random nature of the atomic arrangements in the experimental sample. Notably, the structural features obtained from the 2D projection TEM analysis of Ge25 (Fig. 8(a)) closely resembled the outcomes for the atoms within the a-Ge slab generated using Molecular Dynamics with approximately 4 Å thickness (Fig. 8(b)). Those of the random structures in Figs. 8(c) and (f) were similar to each other, but apparently different from the others. If we can expect the maze pattern in the TEM image of a-Ge to reflect the atomic configuration in a thin slice, the consistency observed between Ge25 and the AIMD simulation models should support the reliability and the accuracy of the TEM-structural features through the TDA approach. The same results were obtained in the case of the point cloud data representing the dark areas in the TEM images (Figs. S3–5, Supplementary Information). Therefore, we need not worry about the flipping bright and dark patterns.

While it is well-acknowledged that the simulation of amorphous materials in AIMD is inherently constrained by a limited phase space, our study has leveraged a comprehensive approach to reduce these limitations. Through comparisons between experimental data and the slices with different thicknesses extracted from an AIMD model, our work demonstrated good agreement in capturing key TEM-structural features. Furthermore, by contrasting our results with those from a random model, we show the non-random nature of our a-Ge samples. These results contribute valuable insights into the structural characteristics and variations within a-Ge, bridging the gap between experimental observations and computational simulations.

D. Correlation analysis between atomic networks and thermal conductivity

Thermal conductivity (k) is defined via the Fourier's law for heat conduction with the temperature gradient (∇T) occurring upon the heat flux (q), $q = -k\nabla T$ application from the contribution of a range of mean free paths of vibrational modes. That is, thermal conductivity depends on the mean free paths (MFPs), which is the mean distance a heat carrier can travel before encountering scattering events. In the case of amorphous materials, the lack of long-range periodicity in the atomic structure complicates the determination of vibrational modes compared to crystalline materials.

Our thermal conductivity measurements for the a-Ge thin films deposited at 25, 100, and 300 °C were 1.10, 1.28, and 1.50 W/m K, respectively (See Fig. 9). Notably, the thermal conductivity of the 250 nm a-Ge thin films increased with higher deposition temperatures. This finding indicates that the deposition temperature significantly impacts the thermal properties of amorphous materials.

Our analysis of the TEM-structural features using the TDA revealed that the deposition temperature affects the formation of the larger atomic rings in a-Ge. These larger rings are composed of five or six vertices and play a significant role in enhancing heat transfer through longer atomic chains. To understand this phenomenon, consider N particles constrained to move along a circular ring with a length L, connected by elastic springs that allow for oscillation. The minimum wavevector ($k = 2\pi/L$) of the oscillator is inversely proportional to L. As

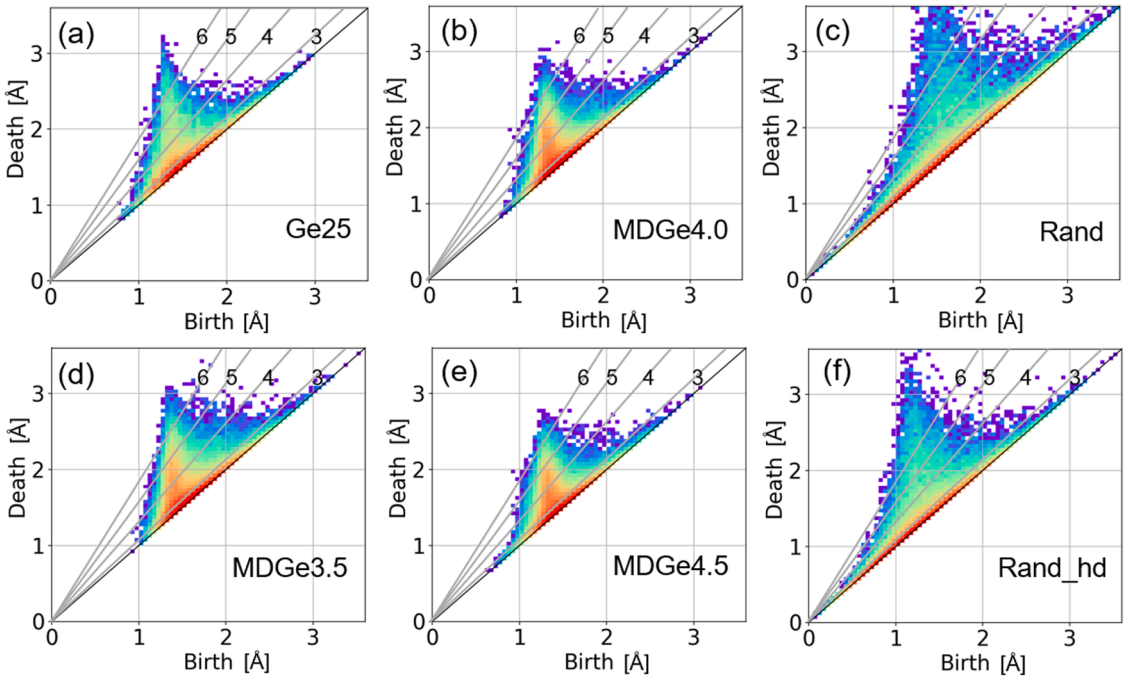

Fig. 7. First-order PDs of (a) Ge25, (b) MDGe4.0, (c) Rand, (d) MDGe3.5, (e) MDGe4.5, and (f) Rand_hd. The colors in the PDs that gradually decrease from red to purple correspond to the density of the birth–death pairs. The comparison of the birth–death pairs in the PDs between Ge25 and the AIMD simulation models depicted in (b), (d), and (e) reveals striking similarities. In contrast, the random structures shown in (c) and (f) exhibit significantly broader distributions of the birth–death pairs. This indicates a close resemblance in the local atomic arrangements between the experimental Ge25 sample and the AIMD simulation models. (For interpretation of the references to colour in this figure legend, the reader is referred to the web version of this article.)

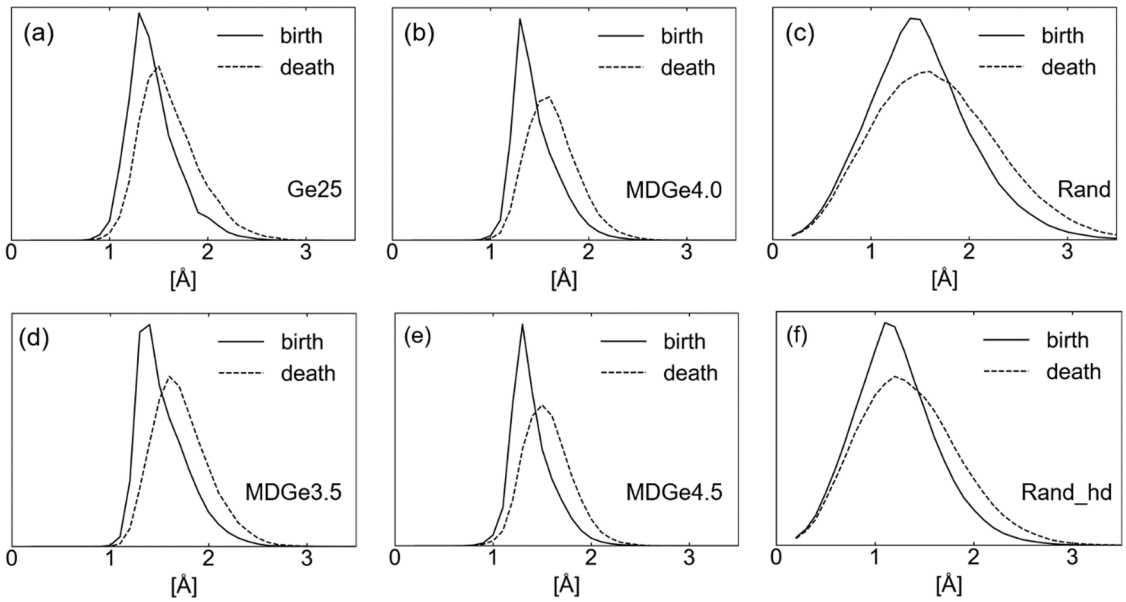

Fig. 8. Analysis of the birth–death values in the first-order PDs for (a) Ge25, (b) MDGe4.0, (c) Rand, (d) MDGe3.5, (e) MDGe4.5, and (f) Rand_hd. The y-axis shows the number of rings at the given birth (or death) value. In Figs. 8a-f, the scale of y-axis is respective to compare the shape of distributions. The TEM-structural feature of (a) demonstrates narrower value ranges for birth and death compared to the random structures of (c) and (f), providing compelling evidence for the non-random nature of the atomic arrangements in a-Ge.

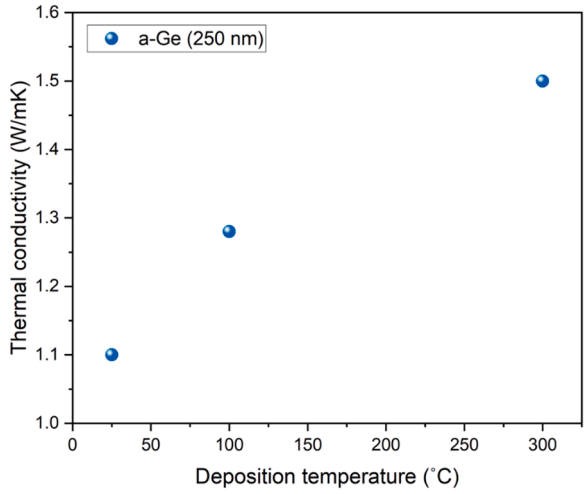

Fig. 9. Relationship between thermal conductivity and deposition temperature for a-Ge thin films.

L increases, the minimum wavevector decreases, leading to lower-frequency oscillations. In simpler terms, the larger ring size corresponds to a reduction in wave frequency. For more detailed insights, you can refer to the reference [39].

The oscillators exhibit distinct mean free paths (MFPs) depending on their frequency [40]. Low-frequency oscillators have longer MFPs, enabling them to travel further without scattering, whereas high-frequency oscillators have shorter MFPs and thus scatter more frequently. This understanding leads to the key concept behind our observations: when larger atomic rings are present in the atomic structure, they lead to a decrease in the frequencies of oscillators and an increase in their MFPs.

This observation is consistent with our previous findings where we identified the contribution of MFPs longer than 100 nm in a-Ge at a higher deposition temperature [37,38]. Furthermore, our previous research demonstrated that factors such as sound velocity and film density were not the primary determinants of high thermal conductivity; instead, short-range order and longer MFPs in a-Ge played crucial roles.

Therefore, we can reasonably infer that the thermal conductivity is enhanced due to the longer MFPs and lower frequencies associated with these larger atomic rings. The birth–death pair distribution in the PDs further supported this observation. That is, the higher deposition temperatures resulted in a broader peak in the larger birth–death region (Fig. 3(c)), which indicated the emergence of additional structural orders and reinforced the relationship between the larger atomic rings and the enhanced thermal conductivity.

In summary, our current findings using TDA on TEM images build upon our previous results, connecting the emergence of larger atomic rings with the increased MFPs, which are known to contribute significantly to the thermal conductivity of a-Ge. This understanding strengthens the relationship between structural features and thermal transport properties in amorphous materials. In other words, the change in the atomic networks influenced by the deposition temperature is a crucial factor in determining the thermal conductivity of a-Ge.

3. Conclusion

Our proposed approach utilizes the TEM-structural features and the TDA to define the atomic network characteristics of amorphous materials and correlate them with the thermal properties. Comparing the experimental a-Ge samples with the AIMD simulation models allowed us to gain a deeper understanding of the local atomic arrangements and provide evidence of the non-random nature of the atomic structures in a-Ge. Higher deposition temperatures promote the formation of larger ring atomic structures with five or six vertices within the a-Ge samples, emphasizing the significant role of atomic networks in enhancing the thermal conductivity. Using the TDA, this study highlights the potential of the TEM-structural features for exploring atomic arrangements and their impact on thermal conductivity. Furthermore, leveraging the understanding of atomic networks and thermal conductivity can guide the design and engineering of amorphous materials with tailored thermal properties. For various applications, the thermal conductivity can be enhanced or suppressed by manipulating atomic arrangements, introducing specific bonding patterns or interfaces, and incorporating

nanostructuring. These findings contribute to our knowledge on amorphous materials at the atomic scale, paving the way for further advancements in material characterization and design.

We illustrate herein an approach that enables the translation of the observed atomic network in TEM to thermal conductivity. As part of our ongoing research, we recognize the importance of further strengthening the relationship between structural analysis and thermal transport properties. To achieve this, we propose future investigations that may include the density of vibrational states and mean free path spectroscopy. These additional studies will expand our understanding of how the identified structural features correlate with the thermal transport behavior in amorphous materials, contributing to a more comprehensive analysis.

4. Methods

A. Sample preparation and thermal conductivity measurements

The a-Ge thin films used in the experiment were prepared using a laboratory-built combinatorial sputtering system with magnetron sputtering. The substrate temperatures were controlled at 25, 100, and 300 °C. Prior to the Ge deposition, an ~2.3 nm native oxide layer was intentionally retained on the Si substrate. The a-Ge thin films were 250 nm thick. A 100 W sputtering power was applied during the deposition. A 150 nm-thick Au film was deposited on the a-Ge thin films to serve as a laser absorber and a temperature sensor. The thermal conductivity measurements were conducted using the ω method under vacuum conditions (<0.02 Pa) at 25 °C. The Au film was heated by a 405 nm pump laser with an angular frequency (ω). The temperature at the Au film surface was detected using a 635 nm probe laser employing the thermoreflectance technique. The temperature at the Au film surface, $T(0)$, was obtained using Eq. (1) by applying the one-dimensional heat conduction equation to the sample system:

$$\frac{T(0)}{qd_0} = \frac{e^{-i\frac{\pi}{4}}}{\sqrt{2\omega\lambda_2 C_2}} + R_{01} + R_{12} + \left(1-\frac{\lambda_0 C_0}{\lambda_2 C_2}\right)\frac{d_0}{\lambda_0} + \left(1-\frac{\lambda_1 C_1}{\lambda_2 C_2}\right)\frac{d_1}{\lambda_1} \quad (1)$$

where, d represents the film thickness; q is the heat flux; λ denotes the thermal conductivity; and C represents the volumetric heat capacity. Subscripts 0, 1, and 2 denote the Au film, a-Ge thin film, and Si substrate, respectively. The sum of the thermal resistances at the Au/a-Ge and a-Ge/Si substrate interfaces is denoted by R_{01} and R_{12}, respectively. The measurements were conducted over the 6 to 48 kHz frequency range. We observed a linear relationship by plotting $\frac{T(0)}{qd_0}$ against $\frac{1}{\sqrt{\omega}}$. The intercept R at $\frac{1}{\sqrt{\omega}} = 0$ corresponded to the sum of the second to fifth terms on the right-hand side of Eq. (1). The thermal conductivity was measured at three different locations on each sample, with each measurement repeated thrice to minimize errors. The details for calculating the thermal conductivities could be found in our previous work [37]. The a-Ge thin film microstructure was characterized through high-resolution transmission electron microscopy (9000NAR, Hitachi Corp.).

B. Topological data analysis

We performed the TDA using the HomCloud software package [41], which is useful in calculating the persistent homology of the pixel data (e.g., TEM images) or the point cloud data (e.g., atomic configurations). It created simplicial complexes from the given discrete data and calculated the persistent homology by applying a filtration process.

We applied the TDA in two different ways. First, we generated a set of point cloud data that characterized the bright (or dark) parts in each TEM image. The PD of the given 8-bit grayscale image was calculated in combination with the level set method. A 5 px Gaussian blur was applied before the calculation. The death positions of the birth–death pairs, whose lifetime |d–b| was larger than 10, appropriately represented the bright (superlevel set) and dark (sublevel set) parts. Next, we performed the TDA of the point cloud data to make a quantitative comparison of the Ge25, Ge100, and Ge300 TEM images. The first-order persistence diagram (PD1) was used to analyze the ring structure. For the birth–death pairs, whose lifetime was larger than 0.2 Å, each PD1 was divided into a 2D mesh (size = 0.2 Å) and converted to a vector. PCA was performed to the vector set. Inverse analysis of the first principal component (PC1) vector was conducted by coloring the center of the death triangle for each birth–death pair. The colors represent the signs of the PC1 vector elements.

C. AIMD simulation

The atomic structure of the amorphous Ge utilized herein was generated through the first-principles MD calculation using VASP [42–46] with a melt–quench method. The simulation employed a cubic cell (L = 28.4 Å) with periodic boundary conditions encompassing 1000 Ge atoms with the PAW potential, 150 eV cut-off energy, and PBE functional. The NVT ensemble with a Nosé–Hoover thermostat was applied for the AIMD calculations. The initial random structure was heated at 575 K for 4.0 ps and quenched at 0 K (structure optimized). The 2D projections of the sliced a-Ge models with 3.5, 4.0, and 4.5 Å thicknesses were obtained to generate the point cloud data for comparison with the TEM samples. The atomic coordinates of the amorphous structures were visualized by VESTA [47].

Code availability

The code used in this study is available upon request from the corresponding author.

CRediT authorship contribution statement

Yen-Ju Wu: Investigation, Writing – original draft, Writing – review & editing. **Kazuto Akagi:** Conceptualization, Methodology, Investigation, Visualization, Writing – review & editing. **Masahiro Goto:** Methodology, Investigation, Writing – review & editing. **Yibin Xu:** Conceptualization, Investigation, Writing – review & editing.

Declaration of Competing Interest

The authors declare that they have no known competing financial interests or personal relationships that could have appeared to influence the work reported in this paper.

Data availability

Data will be made available on request.

Acknowledgments

This work was supported by Japan Science and Technology Agency (JST) CREST Grant Number JPMJCR21O2. A part of this work was supported by Grant-in-Aid for Transformative Research Areas (A) 22H05109 and Grant-in-Aid for Scientific Research (A) 20H00119 by JSPS, Japan.

Supplementary materials

Supplementary material associated with this article can be found, in the online version, at doi:10.1016/j.ijheatmasstransfer.2023.125012.

References

[1] M.J. Mirshojaeian Hosseini, R.A. Nawrocki, A review of the progress of thin-film transistors and their technologies for flexible electronics, Micromachines (Basel) 12 (6) (2021).
[2] H.J. Jang, K. Joong Lee, K.W. Jo, H.E. Katz, W.J. Cho, Y.B. Shin, Top-down fabrication and enhanced active area electronic characteristics of amorphous oxide nanoribbons for flexible electronics, Sci. Rep. 7 (1) (2017) 5728.
[3] M. Kimura, Y. Shibayama, Y. Nakashima, Neuromorphic chip integrated with a large-scale integration circuit and amorphous-metal-oxide semiconductor thin-film synapse devices, Sci. Rep. 12 (1) (2022) 5359.
[4] Y.-J. Wu, M. Sasaki, M. Goto, L. Fang, Y. Xu, Electrically conductive thermally insulating Bi–Si nanocomposites by interface design for thermal management, ACS Appl. Nano Mater. 1 (7) (2018) 3355–3363.
[5] B. Shyam, K.H. Stone, R. Bassiri, M.M. Fejer, M.F. Toney, A. Mehta, Measurement and modeling of short and medium range order in amorphous Ta2O5 thin films, Sci. Rep. 6 (2016) 32170.
[6] N.H. Pham, Ö. Vallin, J. Panda, M. Venkata Kamalakar, J. Guo, J. Luo, C. Wen, S.-L. Zhang, Z.-B. Zhang, High thermoelectric power factor of p-type amorphous silicon thin films dispersed with ultrafine silicon nanocrystals, J. Appl. Phys. 127 (24) (2020).
[7] Y. Fujimoto, M. Uenuma, Y. Ishikawa, Y. Uraoka, Analysis of thermoelectric properties of amorphous InGaZnO thin film by controlling carrier concentration, AIP Adv. 5 (9) (2015).
[8] A. Einstein, Über den Einfluß der Schwerkraft auf die Ausbreitung des Lichtes, Ann. Phys. 340 (10) (1911) 898–908.
[9] G.A. Slack, The thermal conductivity of nonmetallic crystals, in, 1979, pp. 1–71.
[10] D.G. Cahill, R.O. Pohl, Heat-flow and lattice-vibrations in glasses, Solid State Commun. 70 (10) (1989) 927–930.
[11] D.G. Cahill, S.K. Watson, R.O. Pohl, Lower limit to the thermal conductivity of disordered crystals, Phys. Rev. B Condens. Matter 46 (10) (1992) 6131–6140.
[12] P.B. Allen, J.L. Feldman, Thermal conductivity of disordered harmonic solids, Phys. Rev. B Condens. Matter 48 (17) (1993) 12581–12588.
[13] P.B. Allen, J.L. Feldman, Thermal conductivity of glasses: theory and application to amorphous Si, Phys. Rev. Lett. 62 (6) (1989) 645–648.
[14] M.T. Agne, R. Hanus, G.J. Snyder, Minimum thermal conductivity in the context of diffuson-mediated thermal transport, Energy Environ. Sci. 11 (3) (2018) 609–616.
[15] P.B. Allen, J.L. Feldman, J. Fabian, F. Wooten, Diffusons, locons and propagons: character of atomie yibrations in amorphous Si, Philos. Mag. B 79 (11–12) (2009) 1715–1731.
[16] Z. Zhang, Y. Guo, M. Bescond, J. Chen, M. Nomura, S. Volz, Heat conduction theory including phonon coherence, Phys. Rev. Lett. 128 (1) (2022), 015901.
[17] Z. Zhang, Y. Guo, M. Bescond, J. Chen, M. Nomura, S. Volz, How coherence is governing diffuson heat transfer in amorphous solids, npj Comput. Mater. 8 (1) (2022).
[18] Q. Xi, J. Zhong, J. He, X. Xu, T. Nakayama, Y. Wang, J. Liu, J. Zhou, B. Li, A ubiquitous thermal conductivity formula for liquids, Polym. Glass, Amorphous Solids*, Chin. Phys. Lett. 37 (10) (2020).
[19] D. Huang, J. Zhong, S. Raza, R. Niu, B. Fu, D. Yu, T. Nakayama, J. Liu, J. Zhou, Thermal resistance network model for thermal conductivity of normal liquid helium-4 and helium-3, J. Phys. Condens. Matter 35 (41) (2023).
[20] J.L. Braun, S.W. King, A. Giri, J.T. Gaskins, M. Sato, T. Fujiseki, H. Fujiwara, P. E. Hopkins, Breaking network connectivity leads to ultralow thermal conductivities in fully dense amorphous solids, Appl. Phys. Lett. 109 (19) (2016).
[21] S.W. King, J. Bielefeld, G. Xu, W.A. Lanford, Y. Matsuda, R.H. Dauskardt, N. Kim, D. Hondongwa, L. Olasov, B. Daly, G. Stan, M. Liu, D. Dutta, D. Gidley, Influence of network bond percolation on the thermal, mechanical, electrical and optical properties of high and low-k a-SiC:H thin films, J. Non Cryst. Solids 379 (2013) 67–79.
[22] K. Aryana, D.A. Stewart, J.T. Gaskins, J. Nag, J.C. Read, D.H. Olson, M.K. Grobis, P. E. Hopkins, Tuning network topology and vibrational mode localization to achieve ultralow thermal conductivity in amorphous chalcogenides, Nat. Commun. 12 (1) (2021) 2817.
[23] E. Minamitani, T. Shiga, M. Kashiwagi, I. Obayashi, Relationship between local coordinates and thermal conductivity in amorphous carbon, J. Vac. Sci. Technol. A 40 (3) (2022).
[24] A. Hirata, Y. Hirotsu, T.G. Nieh, T. Ohkubo, N. Tanaka, Direct imaging of local atomic ordering in a Pd-Ni-P bulk metallic glass using Cs-corrected transmission electron microscopy, Ultramicroscopy 107 (2–3) (2007) 116–123.
[25] Y. Hirotsu, T.G. Nieh, A. Hirata, T. Ohkubo, N. Tanaka, Local atomic ordering and nanoscale phase separation in a Pd-Ni-P bulk metallic glass, Phys. Rev. B 73 (1) (2006).
[26] K. Sugiyama, T. Kawamata, T. Muto, Medium range ordering realized in Zr80Pt20 amorphous alloy, J. Phys. Conf. Ser. 809 (2017).
[27] Z. Czigany, L. Hultman, Interpretation of electron diffraction patterns from amorphous and fullerene-like carbon allotropes, Ultramicroscopy 110 (7) (2010) 815–819.
[28] M. Ishimaru, R. Nakamura, Y. Zhang, W.J. Weber, G.G. Peterson, N.J. Ianno, M. Nastasi, Electron diffraction radial distribution function analysis of amorphous boron carbide synthesized by ion beam irradiation and chemical vapor deposition, J. Eur. Ceram. Soc. 42 (2) (2022) 376–382.
[29] J.B. Souza Junior, G.R. Schleder, J. Bettini, I.C. Nogueira, A. Fazzio, E.R. Leite, Pair Distribution Function Obtained from Electron Diffraction: an Advanced Real-Space Structural Characterization Tool, Matter 4 (2) (2021) 441–460.
[30] M. Ishimaru, Electron-beam radial distribution analysis of irradiation-induced amorphous SiC, Nucl. Instrum. Methods Phys. Res., Sect. B 250 (1–2) (2006) 309–314.
[31] F. Chazal, B. Michel, An introduction to topological data analysis: fundamental and practical aspects for data scientists, Front. Artif. Intell. 4 (2021), 667963.
[32] Y. Onodera, S. Kohara, S. Tahara, A. Masuno, H. Inoue, M. Shiga, A. Hirata, K. Tsuchiya, Y. Hiraoka, I. Obayashi, K. Ohara, A. Mizuno, O. Sakata, Understanding diffraction patterns of glassy, liquid and amorphous materials via persistent homology analyses, J. Ceram. Soc. Jpn. 127 (12) (2019) 853–863.
[33] Y. Hiraoka, T. Nakamura, A. Hirata, E.G. Escolar, K. Matsue, Y. Nishiura, Hierarchical structures of amorphous solids characterized by persistent homology, Proc. Natl Acad. Sci. 113 (26) (2016) 7035–7040.
[34] S. Hong, D. Kim, Medium-range order in amorphous ices revealed by persistent homology, J. Phys. Condens. Matter 31 (45) (2019), 455403.
[35] S.S. Sorensen, C.A.N. Biscio, M. Bauchy, L. Fajstrup, M.M. Smedskjaer, Revealing hidden medium-range order in amorphous materials using topological data analysis, Sci. Adv. 6 (37) (2020).
[36] E. Minamitani, T. Shiga, M. Kashiwagi, I. Obayashi, Topological descriptor of thermal conductivity in amorphous Si, J. Chem. Phys. 156 (24) (2022), 244502.
[37] T.Z. Zhan, Y.B. Xu, M. Goto, Y. Tanaka, R. Kato, M. Sasaki, Y. Kagawa, Phonons with long mean free paths in a-Si and a-Ge, Appl. Phys. Lett. 104 (7) (2014).
[38] T.Z. Zhan, Y.B. Xu, M. Goto, Y. Tanaka, R. Kato, M. Sasaki, Y. Kagawa, Thermal conductivity of sputtered amorphous Ge films, AIP Adv. 4 (2) (2014).
[39] C. Kittel, Introduction to Solid State Physics, 8 ed, 2004, p. 110.
[40] Y. He, D. Donadio, G. Galli, Heat transport in amorphous silicon: interplay between morphology and disorder, Appl. Phys. Lett. 98 (14) (2011).
[41] I. Obayashi, T. Nakamura, Y. Hiraoka, Persistent homology analysis for materials research and persistent homology software: HomCloud, J. Phys. Soc. Jpn. 91 (9) (2022).
[42] G. Kresse, J. Hafner, Ab initio molecular dynamics for liquid metals, Phys. Rev. B Condens. Matter 47 (1) (1993) 558–561.
[43] G. Kresse, J. Hafner, Ab initio molecular-dynamics simulation of the liquid-metal-amorphous-semiconductor transition in germanium, Phys. Rev. B Condens. Matter 49 (20) (1994) 14251–14269.
[44] G. Kresse, J. Furthmuller, Efficiency of ab-initio total energy calculations for metals and semiconductors using a plane-wave basis set, Comp. Mater. Sci. 6 (1) (1996) 15–50.
[45] G. Kresse, J. Furthmuller, Efficient iterative schemes for ab initio total-energy calculations using a plane-wave basis set, Phys. Rev. B Condens. Matter 54 (16) (1996) 11169–11186.
[46] G. Kresse, D. Joubert, From ultrasoft pseudopotentials to the projector augmented-wave method, Phys. Rev. B 59 (3) (1999) 1758–1775.
[47] K. Momma, F. Izumi, VESTA 3 for three-dimensional visualization of crystal, volumetric and morphology data, J. Appl. Crystallogr. 44 (6) (2011) 1272–1276.